

Article

Energy Transfer from Pr³⁺ to Gd³⁺ and Upconversion Photoluminescence Properties of Y₇O₆F₉:Pr³⁺, Gd³⁺

Yang Sun, Yangbo Wang *, Chengchao Hu * , Xufeng Zhou, Jigong Hao, Wei Li and Huaiyong Li *

School of Materials Science and Engineering, Liaocheng University, Liaocheng 252059, China

* Correspondence: wangyangbo@lcu.edu.cn (Y.W.); huchengchao@lcu.edu.cn (C.H.); huaiyong.lee@gmail.com (H.L.)

Abstract: Upconversion materials have numerous potential applications in light energy utilization due to their unique optical properties. The use of visible light excitation to obtain ultraviolet emission is a promising technology with broad application prospects, while relevant research is absent. A series of Pr³⁺, Gd³⁺ doped Y₇O₆F₉ phosphors were synthesized by traditional solid-state reaction. X-ray diffraction, scanning electronic microscopy, steady-state photoluminescence spectra, a decay dynamic, and upconversion emission spectra of the samples were studied. Under the excitation of 238 nm, the energy transfer from Pr³⁺ to Gd³⁺ was realized and a strong ultraviolet B emission due to the ⁶P_{7/2} → ⁸S_{7/2} transition of the Gd³⁺ ions was achieved. Under the excitation of a 450 nm blue laser, Pr³⁺ absorbed two blue photons to realize the upconversion process and then transferred the energy to Gd³⁺ to obtain the ultraviolet B emission.

Keywords: upconversion; Y₇O₆F₉; phosphors; energy transfer



Citation: Sun, Y.; Wang, Y.; Hu, C.; Zhou, X.; Hao, J.; Li, W.; Li, H. Energy Transfer from Pr³⁺ to Gd³⁺ and Upconversion Photoluminescence Properties of Y₇O₆F₉: Pr³⁺, Gd³⁺. *Materials* **2022**, *15*, 7680. <https://doi.org/10.3390/ma15217680>

Academic Editors: Toma Stoica and Dirk Poelman

Received: 21 September 2022

Accepted: 27 October 2022

Published: 1 November 2022

Publisher's Note: MDPI stays neutral with regard to jurisdictional claims in published maps and institutional affiliations.



Copyright: © 2022 by the authors. Licensee MDPI, Basel, Switzerland. This article is an open access article distributed under the terms and conditions of the Creative Commons Attribution (CC BY) license (<https://creativecommons.org/licenses/by/4.0/>).

1. Introduction

Upconversion (UC) luminescence refers to the nonlinear process of emitting a high-energy photon when two or more low-energy photons are absorbed. Because of its unique physical and chemical properties, UC luminescence has attracted extensive attention over the past few years. Most of the research on UC is based on the excitation in the infrared region to obtain the emission in the visible region and has made enormous progress, which is widely applied in solar cells, biological imaging, oxygenic photosynthesis, solid-state lasers, fluorescent probes, and photodynamic therapy [1–5]. Taking into account factors, such as conversion efficiency, research on the use of abundant visible energy to realize visible-to-ultraviolet (UV) conversion is relatively lacking. UV radiation refers to electromagnetic waves with wavelengths ranging from 100 nm to 400 nm, which is very significant in physics, medicine, the environment, and other aspects. UV light can be divided into ultraviolet A (UVA), ultraviolet B (UVB), and ultraviolet C (UVC), and their wavelength ranges are 400–315 nm, 315–280 nm, and 280–100 nm, respectively. It is necessary and meaningful to seek a method and mechanism to obtain UV emission. Many researchers have made great efforts to explore UV lasers, using UC luminescent materials and nonlinear crystal technology to obtain deep UV lasers [6–8]. At present, using UVB fluorescent lamps is a common method to treat skin diseases, such as psoriasis, vitiligo, and skin burn. Various studies have shown that the most effective range is in the long wave part of the UVB spectrum, that is, between 305 nm and 315 nm. In addition to phototherapy, UVB also has potential advantages in other areas. Because UVB has the visible-blind feature, UV cameras can detect UVB radiation in indoor-lighting environments and can effectively control the interference of solar light sources. Therefore, it has potential application in the field of optical tagging [9–12]. The use of low-energy light as the excitation light source to obtain high-energy UV emission and broaden the application range of the UV region has important research significance.

For some rare earth ions (RE^{3+}), such as Pr^{3+} , Gd^{3+} , Tb^{3+} , and Ce^{3+} , the emission corresponding to the transition between some energy levels is located in the UV band so it can be used as the UV luminous activator. The emission of Pr^{3+} extends from UV to infrared radiation due to its interaction between abundant 4f energy levels and the 4f5d state. In various phosphors doped with Pr^{3+} ions, the transition of $^3\text{H}_4$ to $^3\text{P}_j$ or $^1\text{D}_2$ and then to the 4f5d state has been realized under visible excitation, and the UV region emission of the 4f5d state has been obtained [6,13–17]. The luminescence properties of Pr^{3+} ions largely depend on the host lattice. An important criterion for realizing the visible-to-UV mechanism is that the 4f5d energy level of Pr^{3+} ions is lower than the $^1\text{S}_0$ energy level, and if the host lattice crystal field causes a band energy that is too high, the second excitation step cannot be achieved [14,16,17]. The Gd^{3+} ion shows an ff transition and a characteristic emission at about 313 nm. Furthermore, it has no absorption in visible light due to its unique energy-level structure. Therefore, reports on Gd^{3+} ions' luminescence are mainly ordinary photoluminescence (PL) under high-energy UV excitation. The 4f5d interconfigurational transition of Pr^{3+} overlaps with the $^8\text{S}_{7/2} \rightarrow ^6\text{D}_j$ transition of Gd^{3+} , which can result in an efficient energy transfer. Thus, the UVB emission of the Gd^{3+} ions excited by visible light can be realized [12,18–20]. The quantum efficiency is determined by the nonradiative process of the host lattice. High phonon vibration will increase the nonradiative relaxation rate and, thus, reduce the quantum efficiency [21]. In contrast, fluoride generally has the advantages of low phonon energy (less than 350 cm^{-1}) and a wide transparent region, but it is less chemically stable, easily oxidized, susceptible to moisture, and difficult to prepare and handle. Oxide has good stability, but its phonon energy is relatively high. Oxyfluorides combine the advantages of fluoride and oxide, have moderate phonon cutoff energy and good chemical stability, and are generally considered an ideal host [22–25]. The $\text{Y}_7\text{O}_6\text{F}_9$ crystal has high photochemical stability and a suitable crystal environment, which has great potential to be used as UV UC laser materials.

In this work, we have synthesized $\text{Y}_7\text{O}_6\text{F}_9:\text{Pr}^{3+}$, Gd^{3+} phosphors via the solid-state synthesis method and investigated their optical properties. The energy transfer from Pr^{3+} to Gd^{3+} was analyzed. The UC emission from Gd^{3+} in the UV region upon the excitation of blue light was investigated.

2. Experimental

2.1. Synthesis

$\text{Y}_7\text{O}_6\text{F}_9:\text{Pr}^{3+}$ and $\text{Y}_7\text{O}_6\text{F}_9:\text{Pr}^{3+}$, Gd^{3+} phosphors were synthesized by a traditional solid-state reaction. Stoichiometric amounts of Y_2O_3 , Pr_6O_{11} , and Gd_2O_3 and excessive NH_4F were mixed and ground (the ratio of the rare earth elements to fluorine was 1:2). For the Pr^{3+} and Gd^{3+} doping, a stoichiometric amount of Y^{3+} was omitted. The mixtures were then sintered at $1120\text{ }^\circ\text{C}$ for 30 min in a tube furnace. The samples were cooled down naturally and crushed for further characterization.

2.2. Characterization

The crystal structure of the synthesized samples was identified using powder X-ray diffraction (XRD) analysis by using a Bruker D8 Advance diffractometer and Cu $\text{K}\alpha$ radiation as the incident radiation. The patterns were collected within a 2θ range of 5° – 90° . The morphology of the powder was characterized on a Zeiss Merlin Field Emission Scanning Electron Microscope (FE-SEM). Energy-dispersive X-ray spectroscopy (EDS) was performed on the accessories to the FE-SEM. Steady-state emission and excitation spectra were measured on a Hitachi F-7000 fluorescence spectrophotometer using a 150 W xenon lamp as the excitation source. Fluorescence decays were collected on an Edinburgh Instruments FS5 fluorescence spectrometer with a μs flash lamp as the excitation source. UC emission spectra were obtained by exciting the sample with a 450 nm continuous wave (CW) laser with a maximum output power of 2 W (Changchun New Industries Optoelectronics Technology, Changchun, China).

3. Results and Discussion

3.1. Phase and Structure Analysis

The XRD patterns of the $Y_7O_6F_9:Pr^{3+}, Gd^{3+}$ powders are presented in Figure 1a. The diffraction patterns of all the samples agree with the standard card of $Y_7O_6F_9$ (JCPDS No. 801126), and no detectable impurity peaks corresponding to the second phase are observed. The $Y_7O_6F_9$ crystal structure is highly tolerable, and a solid solution is formed, despite the great difference in the ionic radius of Y^{3+} and Gd^{3+} . A Rietveld analysis was performed on $Y_7O_6F_9:1.4\%Pr^{3+}, 10\%Gd^{3+}$ by using the GSAS program with the structure parameters as the initial input. The calculated and experimental results, as well as their differences of the $Y_7O_6F_9:1.4\%Pr^{3+}, 10\%Gd^{3+}$ sample, are shown in Figure 1b. The obtained cell parameters of $Y_7O_6F_9:1.4\%Pr^{3+}, 10\%Gd^{3+}$, as well as the reliability, are listed in Table 1. The reliability parameters are $R_{wp} = 8.42\%$, $R_p = 6.39\%$, $\chi^2 = 2.276$, which supports the conclusion that the prepared samples are pure phase.

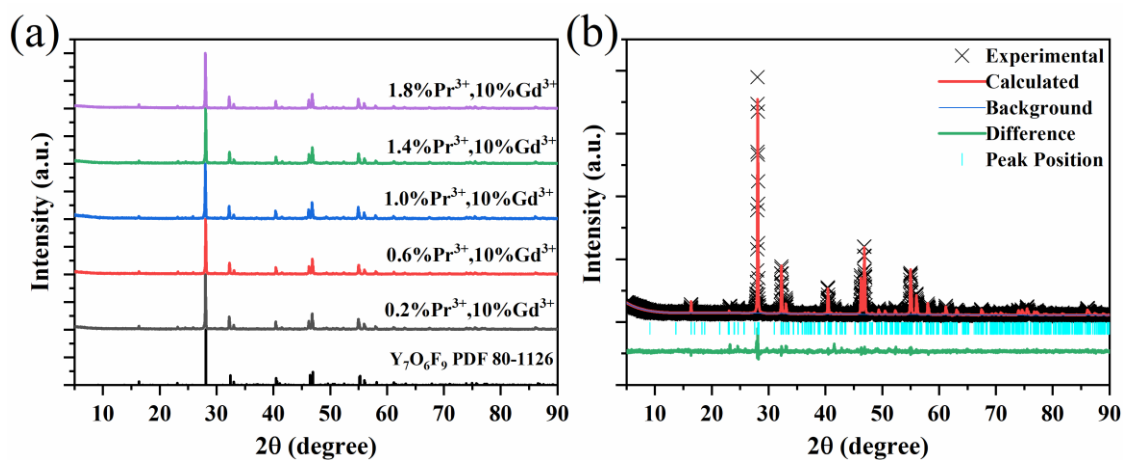


Figure 1. (a) XRD patterns of $Y_7O_6F_9:Pr^{3+}, Gd^{3+}$ phosphors. (b) Results of the Rietveld refinement on $Y_7O_6F_9:1.4\%Pr^{3+}, 10\%Gd^{3+}$.

Table 1. Cell parameters of $Y_7O_6F_9:1.4\%Pr^{3+}, 10\%Gd^{3+}$ obtained from the Rietveld refinement.

Formula	$Y_7O_6F_9$
Crystal system	orthorhombic
Space group	Abm2(39)
Cell parameters	a = 5.4191(1) Å b = 38.8414(8) Å c = 5.5477(1) Å $\alpha = \beta = \gamma = 90^\circ$ V = 1167.702 Å ³
2θ Range	$5^\circ \leq 2\theta \leq 90^\circ$
Reliability factors	$R_{wp} = 8.42\%$ $R_p = 6.39\%$ $\chi^2 = 2.276$

The crystal structure of $Y_7O_6F_9$ was visualized by using Vesta software and is shown in Figure 2. There are four different kinds of Y^{3+} sites, five F^- sites, and four O^{2-} sites in the lattice. The coordination environments of Y^{3+} are also shown in Figure 2. The Y(1) atom is surrounded by six O^{2-} and two F^- atoms in an 8d position, Y(2) by four O^{2-} and three F^- in an 8d position, Y(3) by two O^{2-} and five F^- in an 8d position, and Y(4) is surrounded by eight F^- atoms in a 4c Wyckoff position.

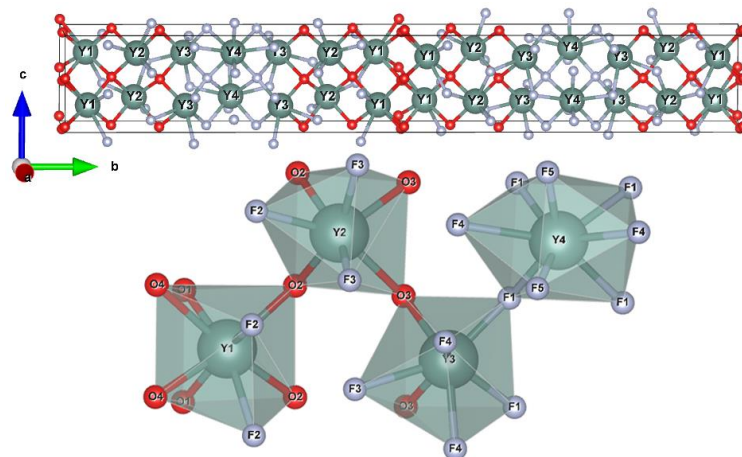


Figure 2. Crystal structure of $Y_7O_6F_9$ (above) and four kinds of coordination for Y^{3+} (below).

3.2. SEM Image of the $Y_7O_6F_9:Pr^{3+}, Gd^{3+}$ Phosphor

In order to examine the surface morphology and average crystal size, an SEM image of $Y_7O_6F_9:1.4\%Pr^{3+}, 10\%Gd^{3+}$ was checked and is shown in Figure 3a. The powder is composed of irregular particles, with an average diameter of about 6.3 μm . The EDS analysis in Figure 3b confirms the existence of Y, O, F, Pr, and Gd elements in the material.

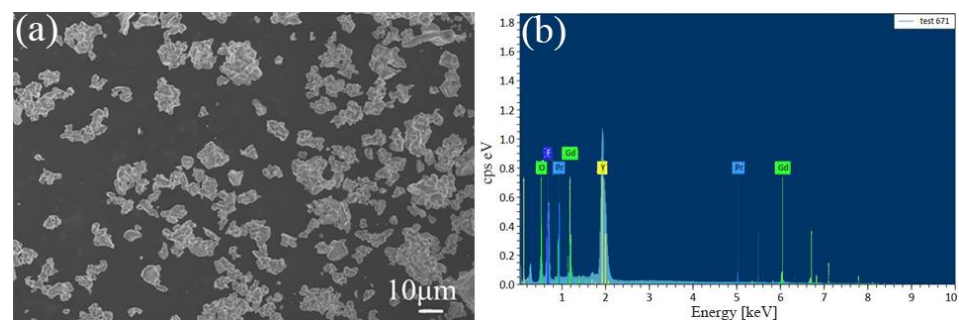


Figure 3. (a) SEM and (b) EDS images of $Y_7O_6F_9:1.4\%Pr^{3+}, 10\%Gd^{3+}$ phosphor.

3.3. PL Properties of the $Y_7O_6F_9:Pr^{3+}$ Phosphor

To investigate the interaction between the Pr^{3+} ions in the $Y_7O_6F_9$ matrix, the excitation and emission spectra of Pr^{3+} in the UV and visible regions were studied. Figure 4a shows the excitation and emission spectra of Pr^{3+} in the UV region. The excitation spectrum was obtained by monitoring the emission at 300 nm. There is an excitation band within the range of 200–250 nm with a maximum of 238 nm, which can be assigned to the $4f^2 \rightarrow 4f5d$ transition of Pr^{3+} . The emission spectra consist of two emission bands with the maxima at 262 nm and 300 nm upon excitation of UV light at 238 nm, which can be attributed to the $4f5d \rightarrow 4f^2$ interconfigurational transition of Pr^{3+} . It can also be observed that the intensity enhanced with the Pr^{3+} concentration, increasing from 0.2 mol% to 1.0 mol%. The excitation spectra shown in Figure 4b are of the emission at 496 nm, which contain two different types of transitions. The narrow line excitation peaks in the visible region are attributed to the $^3H_4 \rightarrow ^3P_{0,1,2}$, 1I_6 transitions of Pr^{3+} . The broad excitation bands centered at 238 nm are due to the transition of $4f^2 \rightarrow 4f5d$. The presence of this band suggests the nonradiative relaxation from the $4f5d$ state to the $4f^2$ state. The $4f$ states stoke the emission generated by the 446 nm excitation is measured, as shown in Figure 4c. The strongest peak at 496 nm originated from the transition of $^3P_0 \rightarrow ^3H_4$, indicating that the 3P_0 level is $20,161 \text{ cm}^{-1}$ higher than the 3H_4 level. Upon the excitation of blue light, 3P_J ($J = 0, 1, 2$), or the 1I_6 states, could be populated, while a rapid relaxation generally happens to the 3P_0 state. One can notice that the spectra are dominated by the emission due to $^3P_0 \rightarrow ^3H_4$.

($J = 4, 5, 6$) transition whether the Pr^{3+} doping concentration is 0.2 mol% or 1.0 mol%, and the emission from the ${}^1\text{D}_2 \rightarrow {}^3\text{H}_4$ transition is extremely weak. Figure 4d shows the emission spectra at 450~750 nm upon excitation at 238 nm. The emission is similar to those shown in Figure 4c. It comes from the relaxation of Pr^{3+} to the lower energy level when it is excited by the $4f5d$ state and is then followed by the transition within the $4f^2$ configuration. Through 580 nm of light used to excite the electrons from the ground state ${}^3\text{H}_4$ to the ${}^1\text{D}_2$ level, the spectra show an emission band from 600 nm to 640 nm, as shown in Figure 4e. However, the intensity changes in a manner opposite to Figure 4c; the emission intensity decreases with the increase of the Pr^{3+} ion concentration, indicating that the quenching of the ${}^1\text{D}_2$ state is very severe, which may be caused by two reasons. The ${}^1\text{D}_2$ level can be populated through the ${}^3\text{P}_0 \rightarrow {}^1\text{D}_2$ multi-phonon relaxation and $[{}^3\text{P}_0, {}^3\text{H}_4] \rightarrow [{}^3\text{H}_6, {}^1\text{D}_2]$ cross-relaxation. It is known that the energy range between ${}^3\text{P}_0$ and ${}^1\text{D}_2$ is about 3866cm^{-1} , and the phonon energy of $\text{Y}_7\text{O}_6\text{F}_9$ is lower (about 450cm^{-1}) so that 8.5 phonons are required to achieve relaxation from ${}^3\text{P}_0$ to ${}^1\text{D}_2$. In order for the equivalent phonon number for the multi-phonon relaxation process to occur, it must be less than 4~5 phonons; so, the probability of occurrence is lower. The quenching of the ${}^1\text{D}_2$ energy level may also occur. The $[{}^1\text{D}_2, {}^3\text{H}_4] \rightarrow [{}^1\text{G}_4, {}^3\text{F}_{3,4}]$ transitions yield a population of ${}^1\text{G}_4$ and ${}^3\text{F}_{3,4}$ levels [26–28]. The transition and relaxation between the relevant energy levels mentioned above under 238 nm and 446 nm blue excitations can be explained by the electron populating processes (see Figure 4f).

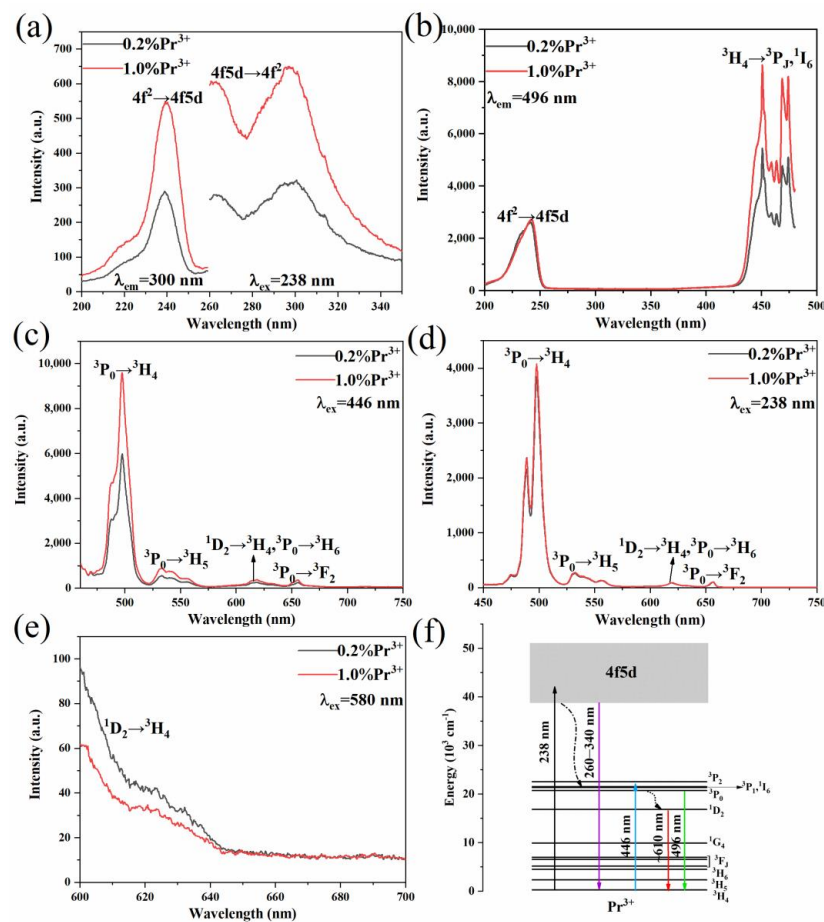


Figure 4. Basic PL properties of $\text{Y}_7\text{O}_6\text{F}_9:\text{xPr}^{3+}$ ($x = 0.2\%$, 1.0%) phosphors. (a) Excitation ($\lambda_{\text{em}} = 300\text{ nm}$) and emission ($\lambda_{\text{ex}} = 238\text{ nm}$) spectra. (b) Excitation spectra ($\lambda_{\text{em}} = 496\text{ nm}$). (c) Emission spectra ($\lambda_{\text{ex}} = 446\text{ nm}$). (d) Emission spectra ($\lambda_{\text{ex}} = 238\text{ nm}$). (e) Emission spectra ($\lambda_{\text{ex}} = 580\text{ nm}$). (f) Energy level diagram of Pr^{3+} . Solid lines represent absorption and emission, and dashed black lines represent nonradiative relaxation.

3.4. PL Properties of the $Y_7O_6F_9:Pr^{3+}, Gd^{3+}$ Phosphor

Figure 5 shows the emission spectra of $Y_7O_6F_9:1.0\%Pr^{3+}, xGd^{3+}$ as a function of the Gd^{3+} concentration. It shows that the intensity of the Gd^{3+} emission increases with the Gd^{3+} content till 10 mol%, and then it drops.

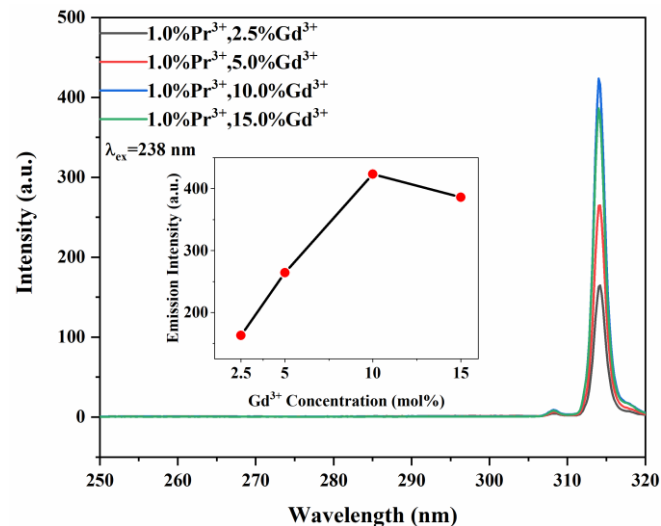


Figure 5. Emission spectra ($\lambda_{ex} = 238$ nm) of $Y_7O_6F_9:1.0\%Pr^{3+}, xGd^{3+}$ ($x = 2.5\%, 5\%, 10\%, 15\%$) phosphors.

Figure 6 illustrates the excitation spectra-monitored emission wavelength at 314 nm. The excitation spectra consist of several excitation peaks of 253 nm, 274 nm, and 276 nm, corresponding to the electronic transition of Gd^{3+} and a broad absorption band from 220 to 250 nm. The broad excitation band can be attributed to the $4f^2 \rightarrow 4f5d$ transition of electrons in the Pr^{3+} ions. The excitation peaks at 253 nm, 274 nm, and 276 nm correspond to the $^8S_{7/2} \rightarrow ^6D_{9/2}$, $^8S_{7/2} \rightarrow ^6I_{11/2}$, $^8S_{7/2} \rightarrow ^6I_{9/2}$ transitions of the Gd^{3+} ions, respectively. Through monitoring the emission of Gd^{3+} , the broad and intense absorption peaks of Pr^{3+} were obtained, and it can be concluded that most of the excitation energy is absorbed by the Pr^{3+} ions.

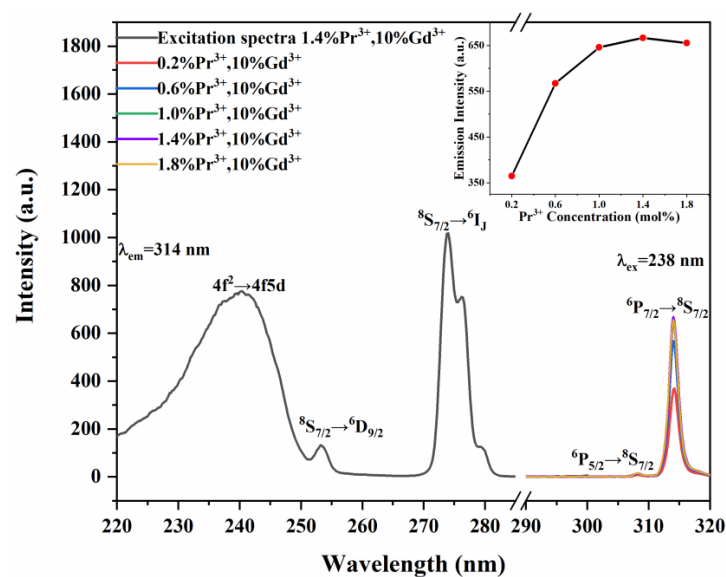


Figure 6. Excitation ($\lambda_{em} = 314$ nm) and emission spectra ($\lambda_{ex} = 238$ nm) of $Y_7O_6F_9:xPr^{3+}, 10\%Gd^{3+}$ ($x = 0.2\%, 0.6\%, 1.0\%, 1.4\%, 1.8\%$) phosphors.

The emission spectra of the $Y_7O_6F_9:xPr^{3+}, 10\%Gd^{3+}$ phosphors in the UV region upon excitation at 238 nm are also shown in Figure 6. The luminescence intensity increases with the increasing Pr^{3+} doping concentration, reaching a maximum at 1.4 mol%, and then it no longer increases, indicating the onset of concentration quenching effects, which can be clearly seen from the inset. From these emission spectra, one can clearly observe the sharp and intense emission peak at 314 nm and a lower intensity peak at 309 nm, which are designated as the ${}^6P_{7/2} \rightarrow {}^8S_{7/2}$ and ${}^6P_{5/2} \rightarrow {}^8S_{7/2}$ transition of Gd^{3+} , respectively. The process is that when the electrons in the Pr^{3+} ions transition to the 4f5d level by absorbing the excitation energy, their energy is transferred to the excitation level of the Gd^{3+} ions. Gd^{3+} relaxes to the ground state and produces UVB emission. It shows that the strategy of energy transfer from Pr^{3+} to Gd^{3+} is effective. Gd^{3+} ions possess an interconfiguration 4f-4f transition and have a wide band gap greater than $30,000\text{ cm}^{-1}$, which reduces the multi-phonon transition [29]. The absence of a broadband emission from the $4f5d \rightarrow 4f^2$ transition for Pr^{3+} also indicates that the energy transfer from Pr^{3+} to Gd^{3+} is efficient.

The fluorescence decay curve of the ${}^3P_0 \rightarrow {}^3H_4$ transition of $Y_7O_6F_9:xPr^{3+}, 10\%Gd^{3+}$ was monitored under the excitation of a 446 nm pulsed xenon lamp, as shown in Figure 7a. It is observed that all the samples show quite similar decay behavior and the decay curves can be well-fitted as a double exponential function. The double exponential model is given below:

$$I_t = A_1 \exp(-t/\tau_1) + A_2 \exp(-t/\tau_2) \quad (1)$$

where I_t is the emission intensity at time t , A_1 and A_2 are constants, and τ_1 and τ_2 are the partial decay lifetimes of the exponential components. The average lifetime, τ , of the 3P_0 level is calculated from the following equation:

$$\tau = (A_1\tau_1^2 + A_2\tau_2^2) / (A_1\tau_1 + A_2\tau_2) \quad (2)$$

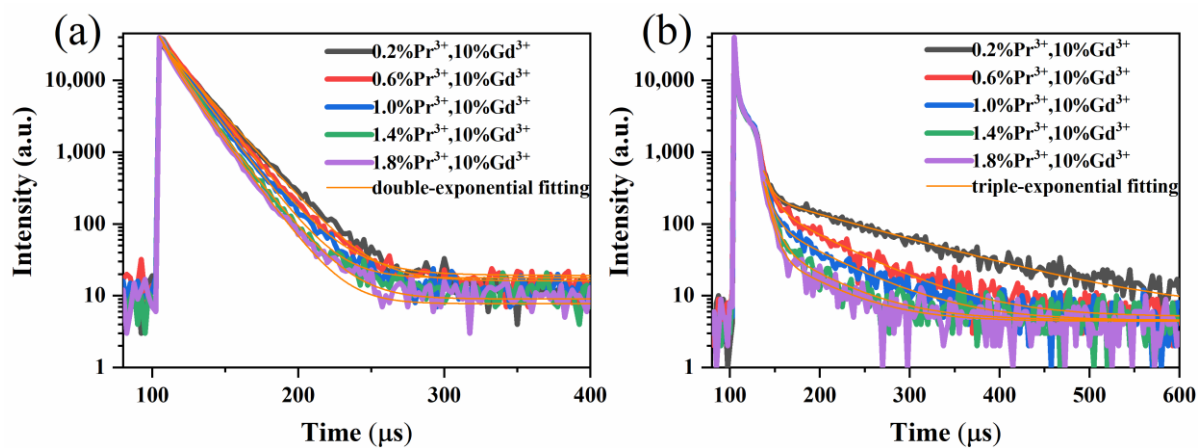


Figure 7. (a) 3P_0 decay curves ($\lambda_{ex} = 446\text{ nm}$, $\lambda_{em} = 496\text{ nm}$). (b) 1D_2 decay curves ($\lambda_{ex} = 580\text{ nm}$, $\lambda_{em} = 602\text{ nm}$) of the $Y_7O_6F_9:xPr^{3+}, 10\%Gd^{3+}$ ($x = 0.2\%, 0.6\%, 1.0\%, 1.4\%, 1.8\%$) phosphors.

The fluorescence lifetime values are given in Table 2 and decreased from $18.8\ \mu\text{s}$ to $13.8\ \mu\text{s}$ with an increasing Pr^{3+} concentration, indicating that the nonradiative relaxation of the Pr^{3+} ions increases. As mentioned above, the multi-phonon relaxation rate is related to the phonon energy of the matrix, so the cross-relaxation between adjacent Pr^{3+} ions may be the main reason for the fast decay of the 3P_0 state. In addition, the lifetime of the 1D_2 level was measured under 580 nm of pulse excitation, as shown in Figure 7b, and the curve was fitted by a more complicated triple exponential equation. The triple exponential model is:

$$I_t = A_1 \exp(-t/\tau_1) + A_2 \exp(-t/\tau_2) + A_3 \exp(-t/\tau_3) \quad (3)$$

Table 2. The calculated lifetimes for 3P_0 decay and 1D_2 decay.

Samples	3P_0 lifetimes in μs	1D_2 lifetimes in μs
0.2%Pr $^{3+}$, 10%Gd $^{3+}$	18.84(2)	132.40(1)
0.6%Pr $^{3+}$, 10%Gd $^{3+}$	17.21(9)	58.11(2)
1.0%Pr $^{3+}$, 10%Gd $^{3+}$	15.89(1)	54.71(1)
1.4%Pr $^{3+}$, 10%Gd $^{3+}$	14.40(6)	41.10(7)
1.8%Pr $^{3+}$, 10%Gd $^{3+}$	13.78(2)	28.45(2)

The average lifetime, τ , of the 1D_2 fluorescence was obtained applying the following expression:

$$\tau = (A_1\tau_1^2 + A_2\tau_2^2 + A_3\tau_3^2) / (A_1\tau_1 + A_2\tau_2 + A_3\tau_3) \quad (4)$$

The lifetime values are also given in Table 2. It can be seen that the lifetime value of 1D_2 is much longer than that of the 3P_0 state, which is due to its own singlet spin multiplicity and spin-forbidden transition [27]. With the increase of the Pr $^{3+}$ ion concentration, the lifetime value also shows a sharp decrease trend. It may be that the $[^1D_2, ^3H_4] \rightarrow [^1G_4, ^3F_{3,4}]$ cross-relaxation process between the Pr $^{3+}$ ions leads to an increase in the 1D_2 nonradiative relaxation rate, which leads to a decrease in the lifetime value.

The UC properties of the Y $_7$ O $_6$ F $_9$:1.4%Pr $^{3+}$, 10%Gd $^{3+}$ phosphor were investigated under excitation with a CW blue laser at 450 nm, as shown in Figure 8a. It can be clearly seen that the spectra were dominated by the emission peak of Gd $^{3+}$. Considering that there is no intermediate state between the $^8S_{7/2}$ and $^6P_{7/2}$ states of Gd $^{3+}$, the excitation at 450 nm could not directly excite Gd $^{3+}$, indicating that the energy absorbed by Gd $^{3+}$ comes from the 4f5d energy level of Pr $^{3+}$. Effective UVB emission of Gd $^{3+}$ was obtained by exciting the Pr $^{3+}$ ions, clearly demonstrating that the energy transfer from Pr $^{3+}$ to Gd $^{3+}$ must be very successful. The energy level diagrams of Pr $^{3+}$ and Gd $^{3+}$ and the UC process of the material system are plotted in Figure 8b. Under blue light excitation, the two-step excitation dominates the UC process. The first excitation brings Pr $^{3+}$ from the ground state, 3H_4 , to the excited state, 3P_1 . A rapid relaxation happens to the 3P_0 state and then Pr $^{3+}$ is excited from the intermediate state to the higher energy 4f5d state. The Gd $^{3+}$ ions can extract the excitation energy of Pr $^{3+}$ to transition to the ground state.

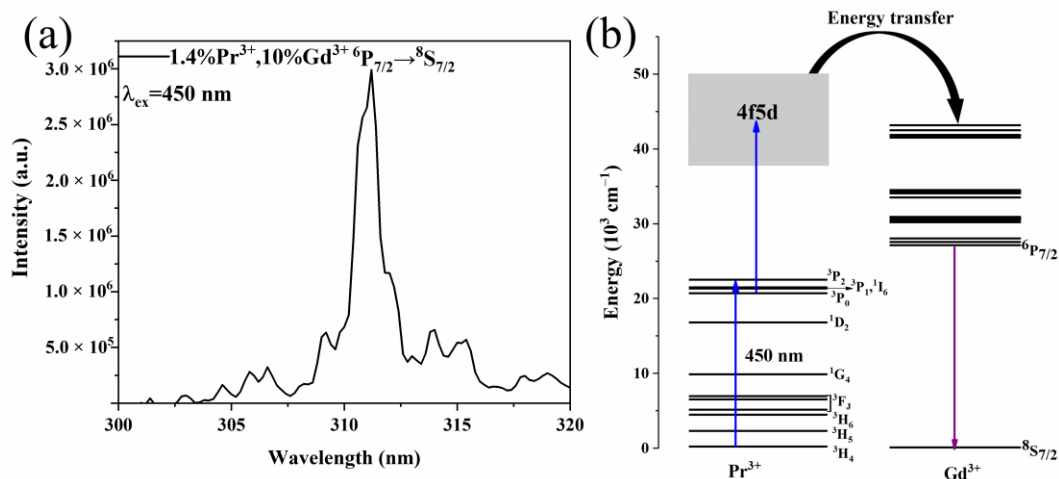


Figure 8. (a) UC Emission spectra ($\lambda_{\text{ex}} = 450 \text{ nm}$) of the Y $_7$ O $_6$ F $_9$:1.4%Pr $^{3+}$, 10%Gd $^{3+}$. The output power was 0.38 W. (b) UC energy transfer mechanism of Pr $^{3+}$ to Gd $^{3+}$.

4. Conclusions

In conclusion, Y $_7$ O $_6$ F $_9$ doped with Pr $^{3+}$ and Gd $^{3+}$ phosphors were successfully synthesized by the traditional solid-state reaction method. XRD data of the Y $_7$ O $_6$ F $_9$ phosphor

are in good agreement with the standard JCPDS data. SEM images showed the agglomeration of irregular particles, and EDS confirmed the presence of all the elements in the phosphor. Through an efficient energy transfer from Pr^{3+} to Gd^{3+} , a strong narrow-band UVB emission from the Gd^{3+} ion could be obtained under 238 nm of excitation. Under blue laser excitation at 450 nm, the UVB emitting of the Gd^{3+} ions was obtained, which originated from Pr^{3+} absorbing two blue photons to the 4f5d configuration, followed by an energy transfer to Gd^{3+} . Our findings suggest that $\text{Y}_7\text{O}_6\text{F}_9:\text{Pr}^{3+}, \text{Gd}^{3+}$ is a promising candidate for visible-to-UV phosphors and opens up new options for applications requiring UV radiation, such as phototherapy treatments and optical tagging.

Author Contributions: Conceptualization, Y.S., Y.W., X.Z. and H.L.; investigation, Y.S., Y.W., H.L. and J.H.; resources, Y.S., Y.W., C.H., H.L. and W.L.; writing—original draft, Y.S.; writing—review and editing, Y.S., Y.W. and X.Z.; supervision, J.H., W.L. and H.L.; funding acquisition, Y.W., C.H. and H.L. All authors have read and agreed to the published version of the manuscript.

Funding: This research was financially supported by the National Natural Science Foundation of China (Grant Nos. NSFC, 12004148, 51701091) and the Natural Science Foundation of Shandong Province (Grant Nos. ZR2021QA057). Innovation Team of Higher Educational Science and Technology Program in Shandong Province (No. 2019KJA025).

Institutional Review Board Statement: Not applicable.

Informed Consent Statement: Not applicable.

Data Availability Statement: Not applicable.

Conflicts of Interest: The authors declare no conflict of interest.

References

1. Wang, H.Q.; Batentschuk, M.; Osvet, A.; Pinna, L.; Brabec, C.J. Rare-earth ion doped up-conversion materials for photovoltaic applications. *Adv. Mater.* **2011**, *23*, 2675–2680. [[CrossRef](#)]
2. Kang, D.; Jeon, E.; Kim, S.; Lee, J. Lanthanide-Doped Upconversion Nanomaterials: Recent Advances and Applications. *BioChip. J.* **2020**, *14*, 124–135. [[CrossRef](#)]
3. Guo, L.; Wang, Y.; Wang, Y.; Zhang, J.; Dong, P.; Zeng, W. Structure, enhancement and white luminescence of multifunctional $\text{Lu}_6\text{O}_5\text{F}_8:20\%\text{Yb}^{3+}, 1\%\text{Er}^{3+}(\text{Tm}^{3+})$ nanoparticles via further doping with Li^+ under different excitation sources. *Nanoscale* **2013**, *5*, 2491–2504. [[CrossRef](#)] [[PubMed](#)]
4. Duan, C.; Liang, L.; Li, L.; Zhang, R.; Xu, Z.P. Recent progress in upconversion luminescence nanomaterials for biomedical applications. *J. Mater. Chem. B* **2018**, *6*, 192–209. [[CrossRef](#)] [[PubMed](#)]
5. do Nascimento, J.P.C.; do Carmo, F.F.; Façanha, M.X.; Sales, J.C.; Gouveia, D.X.; de Andrade, H.D.; Queiroz Júnior, I.S.; Sombra, A.S.B. Up-Conversion Luminescence of $\text{Er}^{3+}/\text{Pr}^{3+}/\text{Yb}^{3+}$ Co-doped LaNbO_4 Phosphors. *J. Electron. Mater.* **2020**, *49*, 6009–6015. [[CrossRef](#)]
6. Wu, J.; Zheng, H.; Liu, X.; Han, B.; Wei, J.; Yang, Y. UVC upconversion material under sunlight excitation: $\text{LiYF}_4:\text{Pr}^{3+}$. *Opt. Lett.* **2016**, *41*, 792–795. [[CrossRef](#)]
7. Espinoza, S.; Volhard, M.F.; Kätker, H.; Jenneboer, H.; Uckelmann, A.; Haase, M.; Müller, M.; Purschke, M.; Jüstel, T. Deep Ultraviolet Emitting Scintillators for Biomedical Applications: The Hard Way of Downsizing $\text{LuPO}_4:\text{Pr}^{3+}$. *Part. Part. Syst. Char.* **2018**, *35*, 1800282. [[CrossRef](#)]
8. Reichert, F.; Moglia, F.; Metz, P.W.; Arcangeli, A.; Marzahl, D.T.; Veronesi, S.; Parisi, D.; Fechner, M.; Tonelli, M.; Huber, G. Prospects of Holmium-doped fluorides as gain media for visible solid state lasers. *Opt. Mater. Express.* **2014**, *5*, 88–101. [[CrossRef](#)]
9. Berneburg, M.; Rocken, M.; Benedix, F. Phototherapy with narrowband vs. broadband UVB. *Acta. Derm. Venereol.* **2005**, *85*, 98–108.
10. Parrish, J.A.; Jaenicke, K.F. Action spectrum for phototherapy of psoriasis. *J. Investig. Dermatol.* **1981**, *76*, 359–362. [[CrossRef](#)]
11. Tamboli, S.; Nair, G.B.; Dhoble, S.J.; Burghate, D.K. Energy transfer from Pr^{3+} to Gd^{3+} ions in $\text{BaB}_8\text{O}_{13}$ phosphor for phototherapy lamps. *Phys. B Condens. Matter* **2018**, *535*, 232–236. [[CrossRef](#)]
12. Yan, S.; Liu, F.; Zhang, J.; Wang, X.-J.; Liu, Y. Persistent Emission of Narrowband Ultraviolet-B Light upon Blue-Light Illumination. *Phys. Rev. Appl.* **2020**, *13*, 044051. [[CrossRef](#)]
13. Cates, E.L.; Kim, J.-H. Upconversion under polychromatic excitation: $\text{Y}_2\text{SiO}_5:\text{Pr}^{3+}$, Li^+ converts violet, cyan, green, and yellow light into UVC. *Opt. Mater.* **2013**, *35*, 2347–2351. [[CrossRef](#)]
14. Yan, S.; Liang, Y.; Chen, Y.; Liu, J.; Chen, D.; Pan, Z. Ultraviolet-C persistent luminescence from the $\text{Lu}_2\text{SiO}_5:\text{Pr}^{3+}$ persistent phosphor for solar-blind optical tagging. *Dalton. Trans.* **2021**, *50*, 8457–8466. [[CrossRef](#)]

15. Cates, E.L.; Kim, J.H. Bench-scale evaluation of water disinfection by visible-to-UVC upconversion under high-intensity irradiation. *J. Photochem. Photobiol. B* **2015**, *153*, 405–411. [[CrossRef](#)] [[PubMed](#)]
16. Cates, E.L.; Li, F. Balancing intermediate state decay rates for efficient Pr³⁺ visible-to-UVC upconversion: The case of β -Y₂Si₂O₇:Pr³⁺. *RSC. Adv.* **2016**, *6*, 22791–22796. [[CrossRef](#)]
17. Cates, E.L.; Wilkinson, A.P.; Kim, J.-H. Visible-to-UVC upconversion efficiency and mechanisms of Lu₇O₆F₉:Pr³⁺ and Y₂SiO₅:Pr³⁺ ceramics. *J. Lumin.* **2015**, *160*, 202–209. [[CrossRef](#)]
18. Shimizu, Y.; Takano, Y.; Ueda, K. UV emissions in Gd³⁺ doped or Gd³⁺-Pr³⁺ Co-doped III-III perovskite-type RMO₃ (R = Y, La; M = Al, Ga). *Thin. Solid. Films.* **2014**, *559*, 23–26. [[CrossRef](#)]
19. Singh, V.; Srinivas Prasad, M.V.V.K.; Rao, A.S.; Rao, J.L.; Irfan, M. On the ultraviolet B emissions of CaLaB₇O₁₃:Gd³⁺ phosphor. *Optik* **2020**, *217*, 164880. [[CrossRef](#)]
20. Mokoena, P.P.; Nagpure, I.M.; Kumar, V.; Kroon, R.E.; Olivier, E.J.; Neethling, J.H.; Swart, H.C.; Ntwaeaborwa, O.M. Enhanced UVB emission and analysis of chemical states of Ca₅(PO₄)₃OH:Gd³⁺,Pr³⁺ phosphor prepared by co-precipitation. *J. Phys. Chem. Solids* **2014**, *75*, 998–1003. [[CrossRef](#)]
21. Ma, M.; Xu, C.; Yang, L.; Ren, G.; Lin, J.; Yang, Q. Intense ultraviolet and blue upconversion emissions in Yb³⁺-Tm³⁺ codoped stoichiometric Y₇O₆F₉ powder. *Phys. B Condens. Matter* **2011**, *406*, 3256–3260. [[CrossRef](#)]
22. Zaldo, C.; Cascales, C. High thermal sensitivity and the selectable upconversion color of Ln, Yb:Y₆O₅F₈ nanotubes. *Phys. Chem. Chem. Phys.* **2014**, *16*, 23274–23285. [[CrossRef](#)] [[PubMed](#)]
23. Dong, J.; Xiong, H.; Wang, X.; Song, L.; Liu, Y.; Yang, J.; Wu, H.; Yang, C.; Gan, S. Size and morphology-controlled synthesis of vernier yttrium oxyfluoride towards enhanced photoluminescence and white light emission. *New. J. Chem.* **2018**, *42*, 11351–11357. [[CrossRef](#)]
24. Xiang, G.-X.; Wang, G.-J.; Zhang, Z.-J.; Feng, H.; Zhao, J.-T.; Wang, J.; Sun, X.-Y.; Mao, R.-H.; Wang, Y. Multicolor luminescence properties of Ln₇O₆F₉: RE³⁺ (Ln = Y, Lu; RE = Pr, Sm and Eu) nano-rods with bifurcation. *J. Alloys Compd.* **2017**, *692*, 471–477. [[CrossRef](#)]
25. Park, S.; Yang, W.; Park, C.-Y.; Noh, M.; Choi, S.; Park, D.; Jang, H.S.; Cho, S.-H. Up-conversion routines of Er³⁺-Yb³⁺ doped Y₆O₅F₈ and YOF phosphors. *Mater. Res. Bull.* **2015**, *71*, 25–29. [[CrossRef](#)]
26. Saeed, N.A.M.; Coetsee, E.; Swart, H.C. Photoluminescence studies of a YOF phosphor synthesized by the pyrolysis method. *Opt. Mater.* **2019**, *96*, 109331. [[CrossRef](#)]
27. Mahlik, S.; Malinowski, M.; Grinberg, M. High pressure luminescence and time resolved spectra of La₂Be₂O₅:Pr³⁺. *Opt. Mater.* **2011**, *34*, 164–168. [[CrossRef](#)]
28. Zhang, L.; Xia, Y.; Shen, X.; Wei, W. Concentration dependence of visible luminescence from Pr³⁺-doped phosphate glasses. *Spectrochim. Acta A. Mol. Biomol. Spectrosc.* **2019**, *206*, 454–459. [[CrossRef](#)]
29. Binnemans, K.; Görrler-Walrand, C.; Adam, J.L. Spectroscopic properties of Gd³⁺-doped fluorozirconate glass. *Chem. Phys. Lett.* **1997**, *280*, 333–338. [[CrossRef](#)]